

Direct Least-Squares Estimation of Spatiotemporal Distributions from Dynamic SPECT Projections Using a Spatial Segmentation and Temporal B-Splines

Bryan W. Reutter*, *Member, IEEE*, Grant T. Gullberg, *Senior Member, IEEE*, and Ronald H. Huesman, *Senior Member, IEEE*

Abstract—Artifacts can result when reconstructing a dynamic image sequence from inconsistent, as well as insufficient and truncated, cone beam single photon emission computed tomography (SPECT) projection data acquired by a slowly rotating gantry. The artifacts can lead to biases in kinetic model parameters estimated from time-activity curves generated by overlaying volumes of interest on the images. However, the biases in time-activity curve estimates and subsequent kinetic parameter estimates can be reduced significantly by first modeling the spatial and temporal distribution of the radiopharmaceutical throughout the projected field of view, and then estimating the time-activity curves directly from the projections. This approach is potentially useful for clinical SPECT studies involving slowly rotating gantries, particularly those using a single-detector system or body contouring orbits with a multidetector system.

We have implemented computationally efficient methods for fully four-dimensional (4-D) direct estimation of spatiotemporal distributions from dynamic SPECT projection data. Temporal B-splines providing various orders of temporal continuity, as well as various time samplings, were used to model the time-activity curves for segmented blood pool and tissue volumes in simulated cone beam and parallel beam cardiac data acquisitions. Least-squares estimates of time-activity curves were obtained quickly using a workstation. Given faithful spatial modeling, accurate curve estimates were obtained using cubic, quadratic, or linear B-splines and a relatively rapid time sampling during initial tracer uptake. From these curves, kinetic parameters were estimated accurately for noiseless data and with some bias for noisy data. A preliminary study of spatial segmentation errors showed that spatial model mismatch adversely affected quantitative accuracy, but also resulted in structured errors (projected model versus raw data) that were easily detected in our simulations. This suggests iterative refinement of the spatial model to reduce structured errors as an area of future research.

Index Terms—Dynamic single photon emission computed tomography (SPECT), fully four-dimensional (4-D) reconstruction, kinetic parameter estimation.

Manuscript received August 31, 1999; revised March 1, 2000. This work was supported by the National Heart, Lung, and Blood Institute of the U.S. Department of Health and Human Services, under Grants R01-HL50663 and P01-HL25840, and by the Director, Office of Science, Office of Biological and Environmental Research, Medical Sciences Division of the U.S. Department of Energy, under Contract DE-AC03-76SF00098. This work was developed in part using the resources at the U.S. Department of Energy National Energy Research Scientific Computing (NERSC) Center. The Associate Editors responsible for coordinating the review of this paper and recommending its publication were F. J. Beekman and M. A. Viergever. *Asterisk indicates corresponding author.*

*B. W. Reutter and R. H. Huesman are with the Center for Functional Imaging, Lawrence Berkeley National Laboratory, University of California, Berkeley, CA 94720 USA (e-mail: bwreutter@lbl.gov).

G. T. Gullberg is with the Medical Imaging Research Laboratory, Department of Radiology, University of Utah, Salt Lake City, UT 84132 USA.

Publisher Item Identifier S 0278-0062(00)05267-8.

I. INTRODUCTION

THE estimation of time-activity curves and kinetic model parameters directly from projection data is potentially useful for clinical dynamic single photon emission computed tomography (SPECT) studies, particularly in those clinics that have only single-detector systems and, thus, are not able to perform rapid tomographic acquisitions. Even with a three-detector system, a patient study that uses body contouring orbits can take 45–60 s to obtain one full tomographic acquisition. Because the radiopharmaceutical distribution changes while the SPECT gantry rotates, projections at different angles come from different tracer distributions. A dynamic image sequence reconstructed from the inconsistent projections acquired by a slowly rotating gantry can contain artifacts that lead to biases in kinetic parameters estimated from time-activity curves generated by overlaying regions of interest on the images. If cone beam collimators are used and the focal point of the collimators always remains in a particular image plane, additional artifacts can develop in other image planes reconstructed using insufficient projection samples [1]. If the projection samples truncate the patient's body, this can also result in additional image artifacts. To overcome these sources of bias in conventional image-based dynamic data analysis, we and others have been investigating the estimation of time-activity curves and kinetic model parameters directly from dynamic SPECT projection data by modeling the spatial and temporal distribution of the radiopharmaceutical throughout the projected field of view [2].

Building on research by Carson [3] and by Formiconi [4] into direct time-activity curve estimation for regions of interest, we have used simulated data to show that unbiased kinetic parameter estimates for one-compartment models can be obtained directly from parallel beam and cone beam SPECT projections, given the blood input function and the proper segmentation of volumes encompassing the projected field of view [5]–[7]. These simulations systematically incorporated physical effects, such as attenuation (Table I), and led to the development of methods that were used to analyze a dynamic ^{99m}Tc -teboroxime patient study [8]. For this patient study, the blood input function was estimated directly from the projections, and spatial models for the left ventricular myocardium, blood pool, liver, and background tissue were determined by automatically segmenting a dynamic volumetric image sequence reconstructed from the inconsistent projection data.

In related work, Chiao *et al.* [9], [10] have jointly estimated spatial boundaries for myocardial regions of interest and kinetic parameters for one-compartment models from simulated single-

TABLE I

SUMMARY OF PROJECTION GEOMETRIES, PHYSICAL MODELING, AND COMPUTATIONAL COMPLEXITY FOR OUR PREVIOUS WORK [5]–[8] AND THIS WORK. THE ABBREVIATIONS FOR THE GEOMETRIES ARE SSP, SINGLE-SLICE PARALLEL BEAM; MSP, MULTISLICE PARALLEL BEAM; AND C, CONE BEAM. IN SECTION II OF THIS WORK, THE NUMBER OF PROJECTION SAMPLES IS DENOTED BY THE PRODUCT OF FACTORS, IJK , AND THE NUMBER OF LINEAR PARAMETERS IS DENOTED BY THE PRODUCT OF FACTORS, MN

	previous work				this work
	[5]	[6]	[7]	[8]	
projection geometry	SSP	C/MSP	SSP	MSP	C/MSP
input function known	yes	yes	yes	no	no
liver in field of view	no	no	yes	yes	yes
attenuation correction	no	no	yes	yes	yes
point response modeling	no	no	no	no	yes
scatter modeling	no	no	no	no	no
projection samples ($\times 10^6$)	0.072	1.7	0.12	7.6	$IJK = 3.7$
linear parameters	9	9	9	8	$MN = 96$
elements in system matrix \mathbf{F} ($\times 10^6$)	0.65	16	1.0	61	$IJKMN = 350$
multiply-and-adds for $\mathbf{F}^T \mathbf{F}$ ($\times 10^6$)	3.2	78	5.2	270	$IJK \frac{MN(MN+1)}{2} = 17,000$

slice transaxial positron emission tomography (PET) projections, using a blood input function that was estimated from the data. In addition to these methods based on segmented regions and volumes, a number of researchers have reconstructed single-slice and multislice parametric images from SPECT and PET data for a variety of kinetic models [11]–[16].

In our previous work, we formulated a nonlinear estimation problem in which a set of linear parameters was estimated using least squares, given iteratively estimated values for the nonlinear washout parameters for one-compartment kinetic models [5]–[7]. As discussed in Section II and summarized in Table I, the computational resources required for the straightforward solution of the embedded linear least-squares subproblem grow linearly with the number of SPECT projection measurements and are nontrivial by today’s standards for typical patient datasets. In particular, the memory required to analyze a dynamic ^{99m}Tc -teboroxime patient study necessitated the use of a Cray J90 at the National Energy Research Scientific Computing (NERSC) Center [8]. To make matters worse, the computational requirements for the straightforward solution increase quadratically with the number of linear parameters. Thus, a more computationally efficient solution is needed to perform more detailed spatiotemporal modeling and to develop further our direct kinetic parameter estimation methods, using currently available computers.

In this work the primary new development, which we report in Section II, is a computationally efficient method that extends Formiconi’s least-squares algorithm [4] so that fully four-dimensional (4-D) direct spatiotemporal distribution estimation from projections can be performed quickly on a workstation with a modest amount of memory. This method is used with simulated data in Section III to reconstruct time-activity curves for segmented volumes encompassing the projected field of view. This method can be applied to projection data acquired using any collimator or orbit geometry, provided that the data yield a preliminary image reconstruction that can be used to segment the activity distribution within the projected field of view.

The secondary result, which we report in Section III, is a preliminary study of the biases that result from modeling various orders of temporal continuity and using various time samplings when estimating time-activity curves directly from dynamic cone beam and parallel beam SPECT projection data. The effects of spatial segmentation errors are also studied. In Section III-A, piecewise cubic, quadratic, linear, and constant B-splines [17] are used to model the time-activity curves for the blood input, three myocardial volumes of interest, liver, and background tissue in simulated data. Attenuation and geometric point response are modeled, but scatter is not. Segmented volumes encompassing the projected field of view are modeled to contain spatially uniform activity concentrations. In Section III-B, a Monte Carlo simulation is used to study the effects of noisy projections on kinetic parameter estimates for one-compartment models obtained from the spline time-activity curves for the blood input function and the myocardial and liver volumes. This “semidirect” approach, in which compartmental modeling is done subsequent to direct time-activity curve estimation, complements our earlier work, in which compartmental model parameters were estimated directly from projection data [5]–[8]. In Section III-C, the effects of failing to segment myocardial defects and inaccurately localizing the myocardial walls are studied with simulated data.

The methodology presented in Section III builds on the work of Chen *et al.* [18], in which a spline fit to the blood input function and kinetic parameters for a compartmental model were jointly estimated from time-activity curves generated by overlaying regions of interest on a simulated temporal sequence of reconstructed PET images. Nichols *et al.* [19] have also used splines to model the time course of activity in volume elements (voxels) reconstructed from dynamic list mode PET data.

II. COMPUTATIONALLY EFFICIENT ESTIMATION OF SPATIOTEMPORAL DISTRIBUTIONS DIRECTLY FROM PROJECTIONS

Time-varying activity concentrations within volumes of interest encompassing the projected field of view can be modeled

by selecting a set of temporal basis functions capable of representing typical time variations and having desired smoothness properties. For example, to fit the blood input function, Chen *et al.* [18] used five piecewise polynomial spline functions defined over four contiguous time segments. The segments were determined by varying their endpoints in a prescribed fashion and using the set that yielded the smallest weighted sum of squared errors, averaged over 100 simulated data sets. To model the time course of activity in voxels reconstructed from dynamic list mode PET data, Nichols *et al.* [19] first calculated the temporal histogram for the all of the data. Then, segment endpoints for cubic B-splines were defined by selecting a set that yielded approximately equal arc lengths along the resulting time-activity curve. In the simulations in Section III, we use 16 B-splines spanning 15 time segments having geometrically increasing length. The order of the splines and the length of the initial time segment are varied in a prescribed fashion, and the errors in the time-activity curve estimates and the subsequent kinetic model parameter estimates are compared.

Similarly, the spatially nonuniform activity concentration within a particular volume can be modeled by selecting an appropriate set of spatial basis functions defined within the volume. For example, to analyze a ^{99m}Tc -teboroxime patient study, we used indicator functions for the left ventricular myocardium, blood pool, liver, and background tissue [8]. These were determined automatically by applying a 4-D edge detection operator to the dynamic image sequence reconstructed from the inconsistent projection data. In the simulations in Section III, we use indicator functions for the known anatomy of a mathematical phantom.

Given a set of temporal basis functions and sets of spatial basis functions for the volumes, coefficients for the resulting spatiotemporal basis functions can be estimated directly from the projections using the following generalization of Formiconi's algorithm, which was developed for temporally static distributions [4].

The projection of the m th spatial basis function along ray i at angle j is denoted by u_{ij}^m , and the integral of the n th temporal basis function during the time interval associated with angle j of rotation k is denoted by v_{jk}^n . The projection equations can be expressed as

$$p_{ijk} = \sum_{m=1}^M \sum_{n=1}^N a_{mn} u_{ij}^m v_{jk}^n \quad (1)$$

where the p_{ijk} are the modeled projections, the a_{mn} are the linear coefficients associated with the time integrals of the projections of the spatiotemporal basis functions, M is the number of spatial basis functions, and N is the number of temporal basis functions. The criterion that is minimized by varying the linear coefficients a_{mn} associated with the time integrals of the projections of the spatiotemporal basis functions is the weighted sum of squares function

$$\chi^2 = \sum_{i=1}^I \sum_{j=1}^J \sum_{k=1}^K \frac{(p_{ijk}^* - p_{ijk})^2}{W_{ijk}} \quad (2)$$

where the p_{ijk}^* are the measured projections, the W_{ijk} are weighting factors, I is the number of projection rays per angle, J is the number of angles per rotation, and K is the number of rotations. Typically, the weighting factors are either unity for an unweighted fit or the estimated variances of the projections for a weighted fit.

Equations (1) and (2) can be rewritten in matrix form as

$$\mathbf{p} = \mathbf{F}\mathbf{a} \quad (3)$$

and

$$\chi^2 = (\mathbf{p}^* - \mathbf{F}\mathbf{a})^T \mathbf{W} (\mathbf{p}^* - \mathbf{F}\mathbf{a}) \quad (4)$$

respectively, where \mathbf{p} is an IJK element column vector whose $[i + (j-1)I + (k-1)IJ]$ th element is p_{ijk} , \mathbf{F} is an $IJK \times MN$ matrix whose $\{[i + (j-1)I + (k-1)IJ], [m + (n-1)M]\}$ th element is $u_{ij}^m v_{jk}^n$, \mathbf{a} is an MN element column vector whose $[m + (n-1)M]$ th element is a_{mn} , \mathbf{p}^* is an IJK element column vector whose $[i + (j-1)I + (k-1)IJ]$ th element is p_{ijk}^* , and \mathbf{W} is an $IJK \times IJK$ diagonal matrix whose $[i + (j-1)I + (k-1)IJ]$ th diagonal element is $1/W_{ijk}$. The criterion χ^2 is minimized by the vector of spatiotemporal basis function coefficients

$$\hat{\mathbf{a}} = (\mathbf{F}^T \mathbf{W} \mathbf{F})^{-1} \mathbf{F}^T \mathbf{W} \mathbf{p}^*. \quad (5)$$

The covariance matrix for the coefficients $\hat{\mathbf{a}}$ is

$$\text{cov}(\hat{\mathbf{a}}) = (\mathbf{F}^T \mathbf{W} \mathbf{F})^{-1} \mathbf{F}^T \mathbf{W} \text{cov}(\mathbf{p}^*) \mathbf{W} \mathbf{F} (\mathbf{F}^T \mathbf{W} \mathbf{F})^{-1} \quad (6)$$

where $\text{cov}(\mathbf{p}^*)$ is the covariance matrix for the measured projections. Given an estimate of $\text{cov}(\mathbf{p}^*)$, estimates of the statistical uncertainties of the coefficients $\hat{\mathbf{a}}$ are the square roots of the diagonal elements of the covariance matrix given by (6). In general, the errors in the coefficients are correlated and the covariance matrix given by (6) has nonzero elements off the diagonal.

Storing the entire matrix \mathbf{F} and calculating the symmetric matrix $\mathbf{F}^T \mathbf{W} \mathbf{F}$ using straightforward matrix multiplication is computationally inefficient. For example, about 3.7 million projection samples result from a 15-min dynamic SPECT study, such as that simulated in Section III-A, in which data are acquired for 64 transverse \times 32 axial rays per angle ($I = 2048$), $J = 120$ angles per rotation, and one rotation per minute ($K = 15$) (Table I). Fully 4-D direct spatiotemporal distribution estimation using 96 basis functions composed from $M = 6$ spatial and $N = 16$ temporal basis functions, such as these used in the simulations described in Section III-A, involves a matrix \mathbf{F} containing $IJKMN \approx 350$ million elements (Table I). For an unweighted least-squares reconstruction of the spatiotemporal basis function coefficients $\hat{\mathbf{a}}$ (i.e., for \mathbf{W} an identity matrix), calculating the symmetric matrix $\mathbf{F}^T \mathbf{F}$ using straightforward matrix multiplication requires $IJKMN(MN+1)/2 \approx 17$ billion multiply-and-add operations, given \mathbf{F} (Table I). This computational burden is nontrivial for current workstation-class computers and grows worse quickly as either the number M of spatial basis functions or the number N of temporal basis functions increases.

The burden of storing the matrix \mathbf{F} can be reduced significantly by storing instead the spatial basis projection factors u_{ij}^m and the temporal basis integral factors v_{jk}^n and calculating the elements of \mathbf{F} as needed. For $IJM \gg JKN$, this reduces memory usage by a factor of about KN . For the example above with $\{I, J, K, M, N\} = \{2048, 120, 15, 6, 16\}$, this requires storage of only $IJM \approx 1.5$ million u_{ij}^m factors and $JKN \approx 29$ thousand v_{jk}^n factors and reduces memory usage by a factor of about 230.

For an unweighted least-squares reconstruction of the spatiotemporal basis function coefficients $\hat{\mathbf{a}}$ (i.e., for \mathbf{W} an identity matrix), the symmetric $MN \times MN$ matrix $\mathbf{F}^T \mathbf{F}$ can be calculated more efficiently as follows. Denoting the $\{[m + (n - 1)M], [m' + (n' - 1)M]\}$ th element of $\mathbf{F}^T \mathbf{F}$ by $\phi^{mmm'n'}$, we have

$$\phi^{mmm'n'} = \sum_{i=1}^I \sum_{j=1}^J \sum_{k=1}^K u_{ij}^m v_{jk}^n u_{ij}^{m'} v_{jk}^{n'}. \quad (7)$$

Rearranging the summations yields

$$\begin{aligned} \phi^{mmm'n'} &= \sum_{j=1}^J \left[\sum_{i=1}^I u_{ij}^m u_{ij}^{m'} \right] \left[\sum_{k=1}^K v_{jk}^n v_{jk}^{n'} \right] \\ &= \sum_{j=1}^J \mu_j^{mm'} \nu_j^{nn'} \end{aligned} \quad (8)$$

where the factors $\mu_j^{mm'}$ and $\nu_j^{nn'}$ denote the inner products $\sum_{i=1}^I u_{ij}^m u_{ij}^{m'}$ and $\sum_{k=1}^K v_{jk}^n v_{jk}^{n'}$, respectively.

The number of $\mu_j^{mm'}$ factors is $JM(M+1)/2$, the number of $\nu_j^{nn'}$ factors is $JN(N+1)/2$, and the number of $\phi^{mmm'n'}$ factors is $MN(MN+1)/2$. It takes I multiply-and-add operations to calculate each $\mu_j^{mm'}$ factor and K multiply-and-add operations to calculate each $\nu_j^{nn'}$ factor. Given the $\mu_j^{mm'}$ and $\nu_j^{nn'}$ factors, it takes J multiply-and-adds to calculate each of the $\phi^{mmm'n'}$ factors. Thus, the $\phi^{mmm'n'}$ can be calculated using just $J[IM(M+1) + KN(N+1) + MN(MN+1)]/2$ multiply-and-adds. For $I \gg N^2$ and $K < M^2$, this reduces the number of operations by a factor of about KN^2 . For the example above with $\{I, J, K, M, N\} = \{2048, 120, 15, 6, 16\}$, this computationally efficient calculation of $\mathbf{F}^T \mathbf{F}$ requires storage of about 19 000 $\mu_j^{mm'}$ and $\nu_j^{nn'}$ factors and about six million multiply-and-add operations, which is a factor of about 2800 less than that required for straightforward matrix multiplication. For the simulations described in Section III-A, this computationally efficient calculation took about 2.2 s on a 194-MHz MIPS R10000-based Silicon Graphics workstation.

Having addressed the major issues of storing \mathbf{F} and calculating $\mathbf{F}^T \mathbf{F}$, the next computational hurdle is calculating $\mathbf{F}^T \mathbf{p}^*$. This can be done in a relatively straightforward manner using $(I+1)JKMN$ multiply-and-add operations, given the u_{ij}^m and v_{jk}^n factors. The system of equations $\mathbf{F}^T \mathbf{F} \hat{\mathbf{a}} = \mathbf{F}^T \mathbf{p}^*$ can then be solved efficiently for the spatiotemporal basis function coefficients $\hat{\mathbf{a}}$ using the Cholesky decomposition of $\mathbf{F}^T \mathbf{F}$ [20].

An estimate of the covariance matrix for the unweighted least-squares estimates $\hat{\mathbf{a}}$ [(6)] can be calculated in the following computationally efficient manner. From this covariance matrix,

the covariance between integrated segments of the spline models for the time-activity curves for the blood input function and a tissue uptake function can be estimated, which may be useful for obtaining more accurate compartmental parameter estimates via a weighted least-squares fit [21]. In Section III-B, however, an unweighted least-squares fit is performed.

Given an estimate $\hat{\mathbf{P}}$ of the covariance matrix for the measured projections and substituting the identity matrix for \mathbf{W} in (6), we obtain

$$\text{cov}(\hat{\mathbf{a}}) = (\mathbf{F}^T \mathbf{F})^{-1} \mathbf{F}^T \hat{\mathbf{P}} \mathbf{F} (\mathbf{F}^T \mathbf{F})^{-1}. \quad (9)$$

Inverting the symmetric $MN \times MN$ matrix, $\mathbf{F}^T \mathbf{F}$ is straightforward, given its Cholesky decomposition. Taking the measured projections to be independent Poisson random variables, an estimate $\hat{\mathbf{P}}$ of their covariance matrix is the $IJK \times IJK$ diagonal matrix having the estimated projection vector $\hat{\mathbf{p}} = \mathbf{F} \hat{\mathbf{a}}$ along the diagonal. Denoting the $\{[m + (n - 1)M], [m' + (n' - 1)M]\}$ th element of the symmetric $MN \times MN$ matrix $\mathbf{F}^T \hat{\mathbf{P}} \mathbf{F}$ by $\psi^{mmm'n'}$, we have

$$\psi^{mmm'n'} = \sum_{i=1}^I \sum_{j=1}^J \sum_{k=1}^K u_{ij}^m v_{jk}^n \hat{p}_{ijk} u_{ij}^{m'} v_{jk}^{n'} \quad (10)$$

where \hat{p}_{ijk} is the $[i + (j - 1)I + (k - 1)IJ]$ th element of the estimated projection vector $\hat{\mathbf{p}}$. Rearranging the summations yields

$$\begin{aligned} \psi^{mmm'n'} &= \sum_{j=1}^J \sum_{k=1}^K \left[\sum_{i=1}^I u_{ij}^m \hat{p}_{ijk} u_{ij}^{m'} \right] v_{jk}^n v_{jk}^{n'} \\ &= \sum_{j=1}^J \sum_{k=1}^K \omega_{jk}^{mm'} v_{jk}^n v_{jk}^{n'} \end{aligned} \quad (11)$$

where the factor $\omega_{jk}^{mm'}$ denotes the weighted inner product $\sum_{i=1}^I u_{ij}^m \hat{p}_{ijk} u_{ij}^{m'}$.

The number of $\omega_{jk}^{mm'}$ factors is $JKM(M+1)/2$, and the number of $\psi^{mmm'n'}$ factors is $MN(MN+1)/2$. Given the \hat{p}_{ijk} , it takes $2I$ multiply operations and I add operations to calculate each $\omega_{jk}^{mm'}$ factor. Given the $\omega_{jk}^{mm'}$ factors, it takes $2JK$ multiplies and JK adds to calculate each of the $\psi^{mmm'n'}$ factors. Thus, the $\psi^{mmm'n'}$ can be calculated using just $JK[IM(M+1) + MN(MN+1)]$ multiply operations and half that number of add operations. Compared with the computationally efficient calculation of $\mathbf{F}^T \mathbf{F}$, this calculation of $\mathbf{F}^T \hat{\mathbf{P}} \mathbf{F}$ requires about $2K$ times more multiply-and-adds and about K times more memory, given $\hat{\mathbf{P}}$. For the case in which $\hat{\mathbf{P}}$ is the diagonal matrix having the estimated projection vector $\hat{\mathbf{p}} = \mathbf{F} \hat{\mathbf{a}}$ along the diagonal, $\hat{\mathbf{P}}$ can be calculated using $IJKM(N+1)$ multiply-and-add operations, which is about $(N+1)/(M+1)$ times more multiply-and-adds than is needed to calculate $\mathbf{F}^T \hat{\mathbf{P}} \mathbf{F}$. Thus, given the calculation time for $\mathbf{F}^T \mathbf{F}$ of about 2.2 s on a 194-MHz MIPS R10000-based Silicon Graphics workstation and $K = 15$ rotations, such as for the simulations described in Section III-A, calculation of $\mathbf{F}^T \hat{\mathbf{P}} \mathbf{F}$ should take about 1 min, given $\hat{\mathbf{P}}$. For $M = 6$ spatial basis

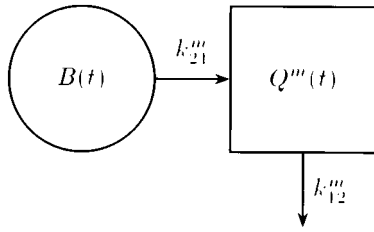


Fig. 1. Compartmental model for ^{99m}Tc -teboroxime in the myocardium. $B(t)$ is the blood input function, $Q^m(t)$ is the tracer in tissue volume m , and k_{21}^m and k_{12}^m are the rate constants for uptake and washout, respectively.

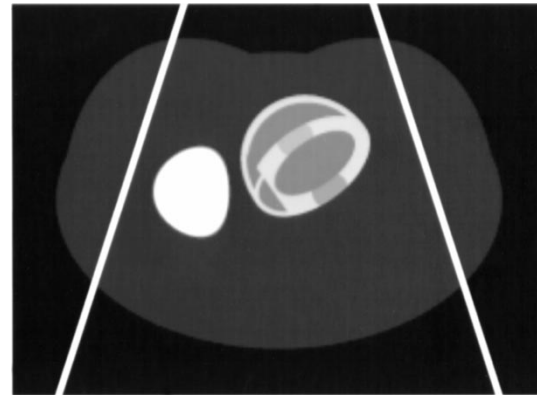
functions and $N = 16$ temporal basis functions, calculation of $\hat{\mathbf{P}}$ should take about 3 min.

For a weighted least-squares reconstruction of the spatiotemporal basis function coefficients $\hat{\mathbf{a}}$ [i.e., for $\mathbf{W}^{-1} = \text{cov}(\mathbf{p}^*)$ in (5) and (6)], calculating $\mathbf{F}^T \mathbf{W} \mathbf{F}$ takes the same amount of computation as calculating $\mathbf{F}^T \hat{\mathbf{P}} \mathbf{F}$. Thus, for dynamic SPECT projection data acquired with a relatively small number of rotations K , it appears that with these methods, a workstation with a modest amount of memory can be used to perform a weighted least-squares reconstruction of the spatiotemporal basis function coefficients $\hat{\mathbf{a}}$, as well as to obtain an estimate of the covariance matrix for the coefficients, in a reasonable amount of time. These methods are easily parallelized, and additional savings in computation can be realized by taking advantage of the sparsity of nonzero spatial basis projection factors w_{ij}^m and nonzero temporal basis integral factors v_{jk}^n .

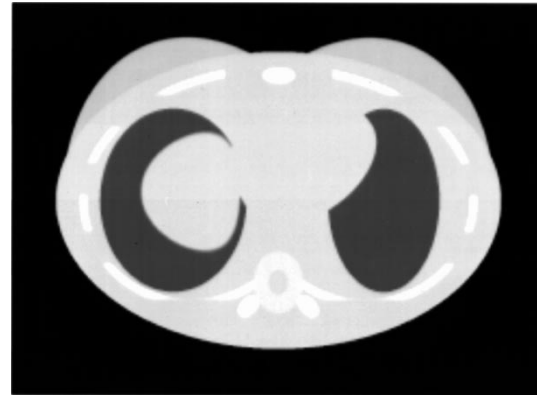
III. COMPUTER SIMULATIONS

The Mathematical Cardiac Torso (MCAT) phantom [22], developed by the University of North Carolina Medical Imaging Research Laboratory, was used in simulations to evaluate the ability to estimate spatiotemporal distributions directly from dynamic cone beam and parallel beam SPECT projections using unweighted least squares. In addition, kinetic parameters for one-compartment models (Fig. 1) were estimated from the resulting spatiotemporal distributions, and a preliminary study of the effects of spatial segmentation errors was performed. The MCAT emission phantom [Fig. 2(a)] was composed of 128 contiguous 1.75-mm thick slices and contained three myocardial volumes of interest (normal myocardium, septal defect, and lateral defect), blood pool, liver, and background tissue. These six volumes did not overlap. The myocardial defects were defined as the intersection of 3-cm diameter spheres with the septal and lateral walls of the left ventricle. Cone beam and parallel beam projections were attenuated using the corresponding MCAT attenuation phantom [Fig. 2(b)]. Single-slice versions of these phantoms were used in our previous work [7].

The simulated time-activity curves for the six emission volumes are shown in Fig. 3. These are the same curves that were used for the single-slice simulation in our previous work [7]. The time-activity curves for the three myocardial volumes of interest and the liver were generated by using the blood pool curve as the input to one-compartment models having kinetics corresponding to those of teboroxime [23]–[25]. The background tissue activity was proportional to the blood pool activity.



(a)



(b)

Fig. 2. Transverse cross sections through (a) the MCAT emission phantom and (b) the MCAT attenuation phantom. The truncation of data resulting from the use of cone beam collimators is depicted in (a).

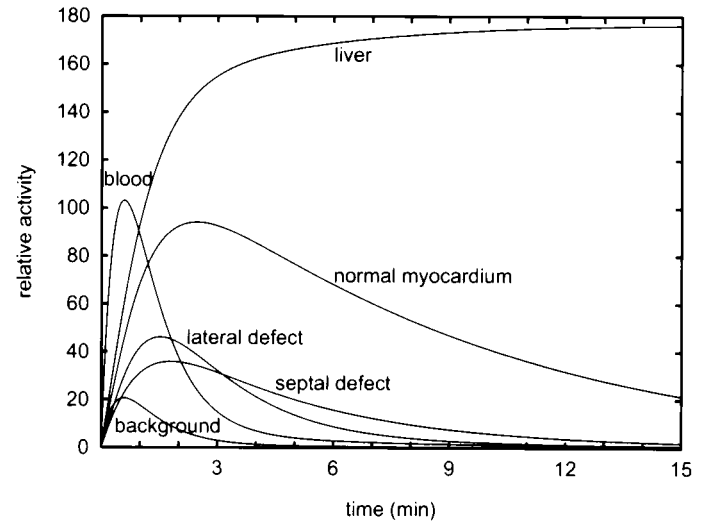


Fig. 3. Simulated time-activity curves for the volumes shown in Fig. 2(a).

The simulated 15-min data acquisition consisted of 64 transverse \times 32 axial rays per angle ($I = 2048$), $J = 120$ angles per rotation, and one rotation per minute ($K = 15$) of a single-detector system. The projection bins were 7 mm \times 7 mm at the detector for both the cone beam and parallel beam geometries, and the detector was 30 cm from the center of the field of view. The collimators had a hole diameter of 2 mm, a length of 4 cm,

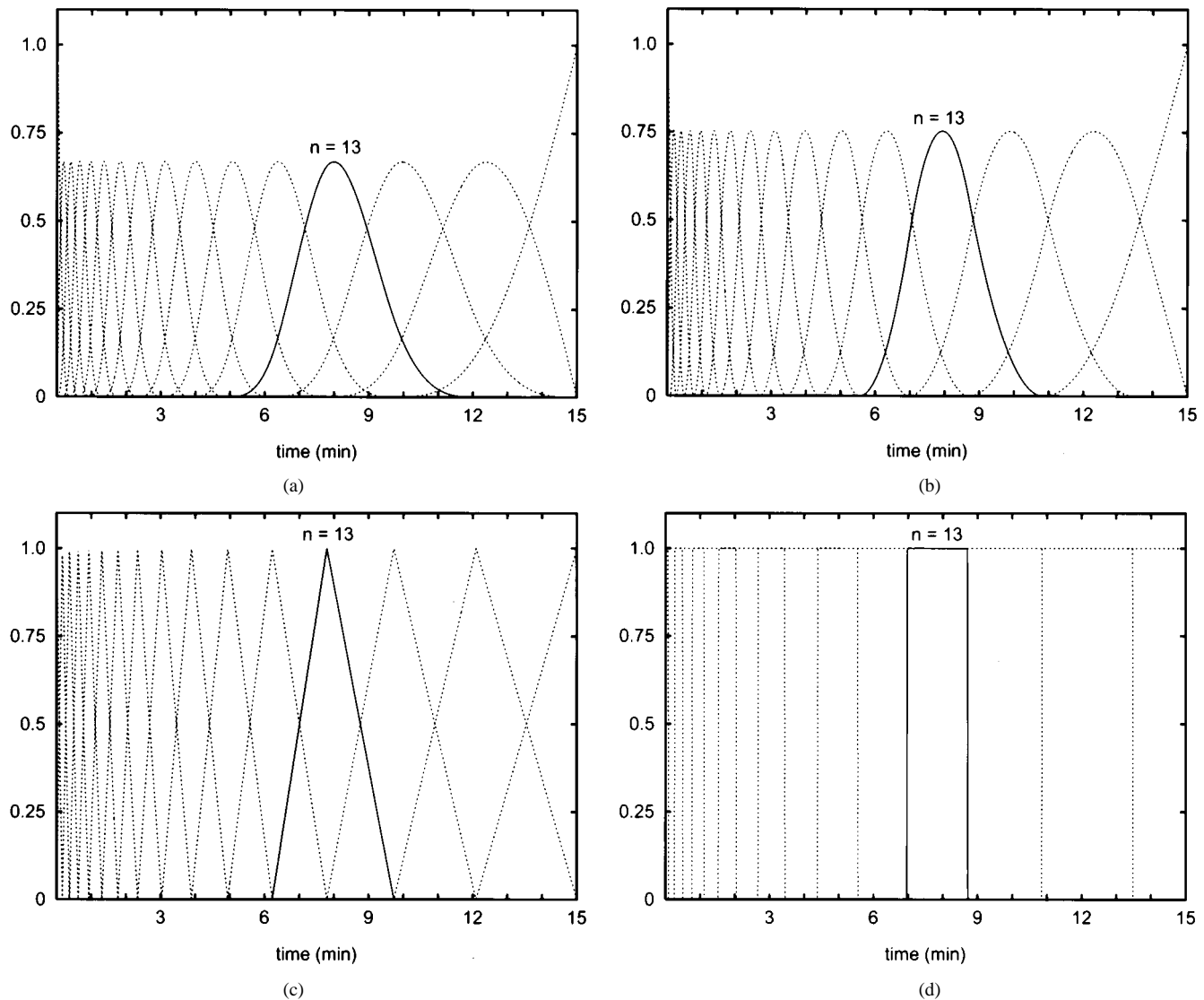


Fig. 4. Examples of piecewise (a) cubic, (b) quadratic, (c) linear, and (d) constant B-spline basis functions used to model time-activity curves. Sixteen splines were used to span 15 time segments having geometrically increasing length. The thirteenth spline is shown as a solid curve. The initial time segment length for the splines shown here is 10 s.

and were offset 1 cm from the detector. The cone beam collimators had a focal length of 70 cm, which resulted in truncation of the data [Fig. 2(a)]. The parallel beam data were not truncated. Attenuation and geometric point response were modeled using a ray-driven projector with line length weighting [26]. Scatter was not modeled.

A. Spatiotemporal Distribution Estimates

The spatial basis projection factors u_{ij}^m were defined by forward projecting each of the six known emission volumes composing the MCAT phantom [Fig. 2(a)]. Each emission volume was modeled to contain spatially uniform activity (i.e., each volume was represented by a spatial indicator function), which yielded $M = 6$ sets of spatial basis projection factors.

The temporal basis integral factors v_{jk}^n were defined by integrating $N = 16$ splines spanning 15 time segments having geometrically increasing length (Fig. 4). Piecewise cubic,

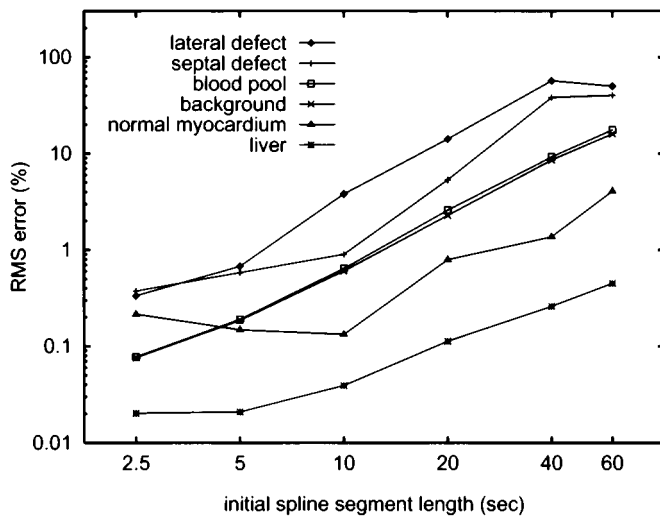
quadratic, linear, and constant B-splines were used with initial time segment lengths ranging between 2.5 and 60 s (Table II). The shorter initial time segment lengths provided a higher density of temporal spline basis functions at the beginning of the simulated acquisition, when the activity concentrations were changing most rapidly (Fig. 3). The 60-s initial time segment length provided basis functions spaced uniformly in time. The cubic, quadratic, and linear B-splines allow modeling of curves that are continuous through their second, first, and zeroth derivative, respectively.

The computational benefits of factoring the matrix \mathbf{F} into the spatial basis projection factors u_{ij}^m and the temporal basis integral factors v_{jk}^n were evident in the simulation. Rather than storing its more than 350 million elements, about 1.5 million u_{ij}^m and v_{jk}^n factors were stored instead. The number of multiply-and-adds used to calculate $\mathbf{F}^T \mathbf{F}$ was reduced from over 17 billion to less than six million. A set of time-activity curves was estimated directly from the 3.7 million simulated projection samples in about 2.3 min on a 194-MHz MIPS R10000-

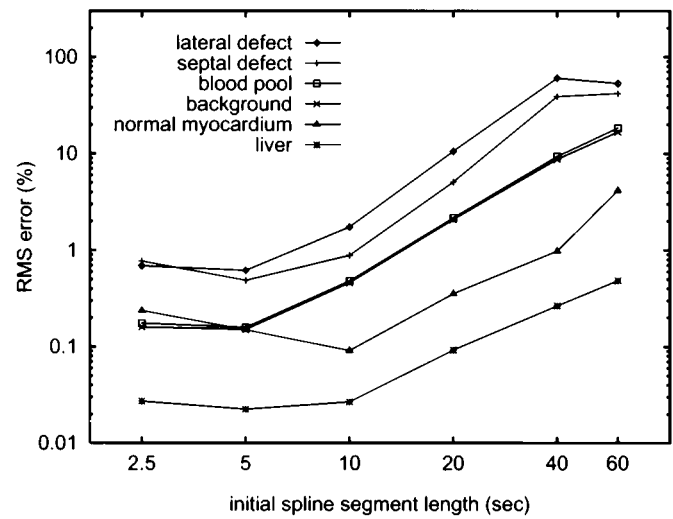
TABLE II

TEMPORAL SAMPLINGS USED IN THE SIMULATIONS IN SECTION III-A. GIVEN AN INITIAL TIME SEGMENT LENGTH, A SCALING FACTOR WAS CALCULATED AND USED TO GENERATE A SEQUENCE OF 15 TIME SEGMENTS HAVING GEOMETRICALLY INCREASING LENGTH AND SPANNING A TOTAL OF 15 MIN

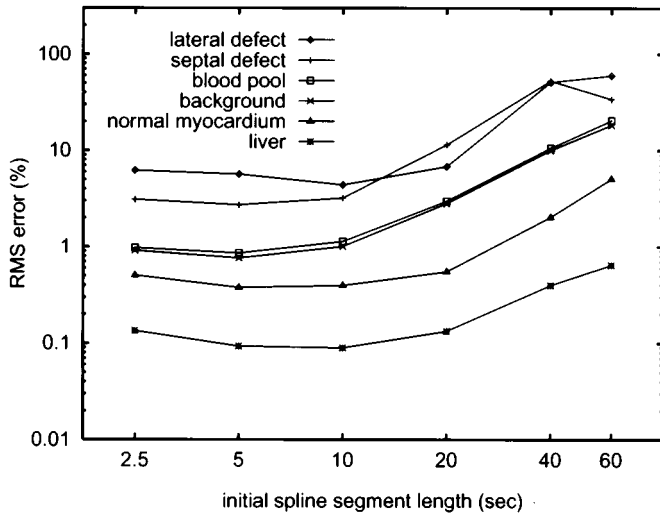
initial time segment (sec)	segment scaling factor	subsequent time segments (sec)													
		2	3	4	5	6	7	8	9	10	11	12	13	14	15
2.5	1.39	3.5	4.8	6.7	9.4	13	18	25	35	49	68	95	130	180	250
5.0	1.31	6.5	8.6	11	15	19	25	33	43	56	74	96	130	170	220
10	1.23	12	15	18	23	28	34	42	51	63	77	95	120	140	170
20	1.14	23	26	30	34	39	45	51	58	67	76	87	100	110	130
40	1.06	42	45	47	50	52	55	58	62	65	69	72	77	81	85
60	1.00	60	60	60	60	60	60	60	60	60	60	60	60	60	60



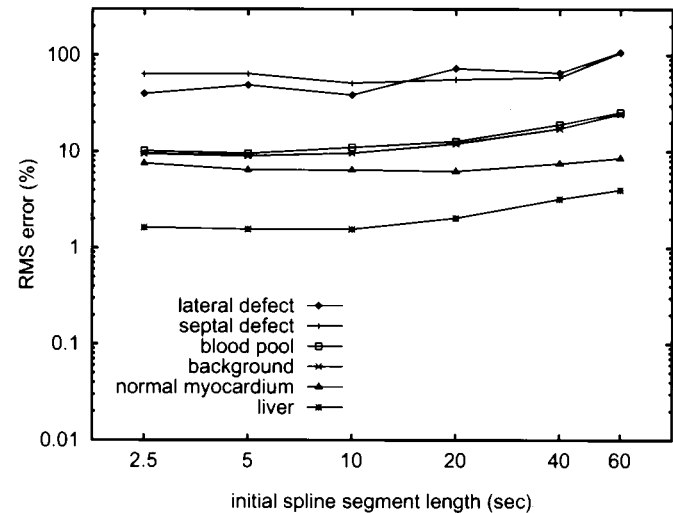
(a)



(b)



(c)



(d)

Fig. 5. Normalized rms modeling errors for time-activity curves estimated directly from noiseless cone beam projections, using piecewise (a) cubic, (b) quadratic, (c) linear, and (d) constant B-spline basis functions (e.g., Fig. 4) and initial time segment lengths ranging between 2.5 and 60 s (Table II).

based Silicon Graphics workstation. The calculations of $\mathbf{F}^T \mathbf{F}$ and $\mathbf{F}^T \mathbf{p}^*$ took about 2.2 s and 2.2 min, respectively.

Figs. 5 and 6 depict the root mean square (rms) differences between the simulated time-activity curves and the spline curves

estimated directly from noiseless projections, normalized by the rms values of the simulated curves and expressed as percentages. The temporal spline modeling errors were largest for the septal and lateral defects, which had relatively small spatial sup-

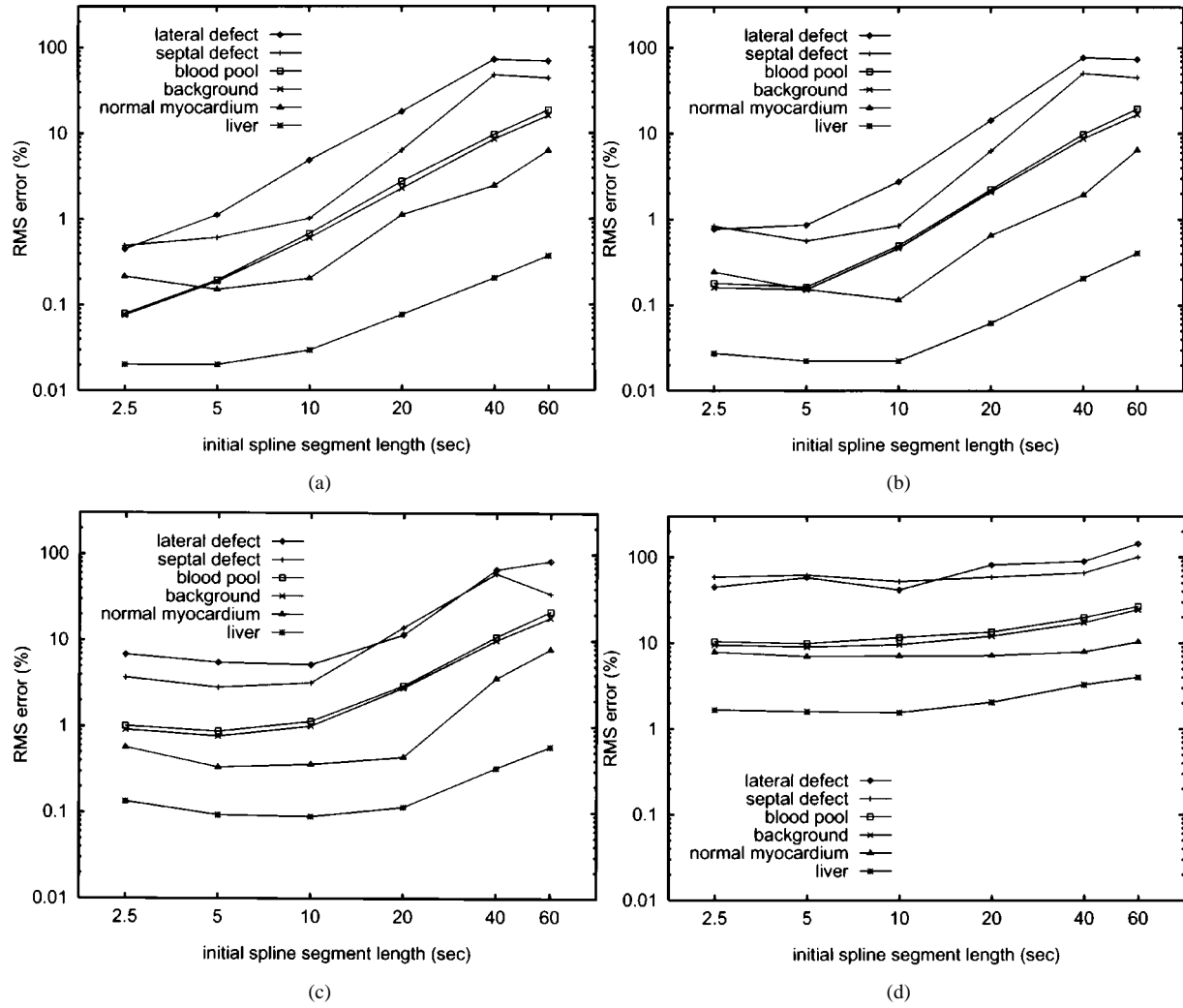


Fig. 6. Same quantities as in Fig. 5, for parallel beam projections.

ports [Fig. 2(a)] and low-activity concentrations (Fig. 3). Intermediate errors resulted for the blood pool and background, which had larger spatial supports but quickly decaying activity concentrations. The errors were smallest for the normal myocardium and liver, which had larger spatial supports and high-activity concentrations throughout the simulated data acquisition. The errors tended to increase as the length of the initial time segment for the splines increased.

In most cases, the temporal spline modeling errors for the three myocardial volumes of interest and the blood pool were smaller for the cone beam geometry than for the parallel beam geometry, because of the increased relative sensitivity to those volumes provided by the cone beam sampling. Errors for the background tissue were comparable for both geometries, whereas in most cases, the errors for the liver were larger for the cone beam geometry. For the cone beam geometry and the relatively rapid initial sampling provided by using initial time segment lengths of 2.5, 5, or 10 s, the errors for all six volumes ranged between 0.020% and 3.8%, 0.022% and 1.7%, 0.090% and 6.2%, and 1.6% and 64% for the cubic, quadratic, linear, and constant B-splines, respectively (Fig. 5). The corresponding ranges of errors for the parallel beam geometry were 0.020%–4.9%, 0.022%–2.7%, 0.089%–6.8%, and 1.6%–62%

(Fig. 6). For the cone beam geometry and the uniform time sampling provided by using an initial time segment length of 60 s, the errors ranged between 0.45% and 50%, 0.48% and 53%, 0.65% and 60%, and 4.0% and 110% for the cubic, quadratic, linear, and constant B-splines, respectively. The corresponding ranges of errors for the parallel beam geometry were 0.37%–69%, 0.41%–73%, 0.58%–83%, and 4.0%–140%.

B. Kinetic Parameter Estimates

Of interest is how the temporal spline modeling errors bias the estimates of kinetic parameters obtained from the directly estimated time-activity curves. To study this, we used the program RFIT [27]–[29] to fit one-compartment kinetic models to the directly estimated time-activity curves for the three myocardial volumes of interest and the liver, using the directly estimated blood pool curve as the input function. The background tissue activity was modeled to be proportional to the blood pool activity, and its amplitude was also estimated.

For the one-compartment kinetic model (Fig. 1), the uptake in tissue volume m is

$$Q^m(t) = k_{21}^m \int_0^t B(\tau) e^{-k_{12}^m(t-\tau)} d\tau = k_{21}^m V^m(t) \quad (12)$$

TABLE III

KINETIC PARAMETERS OBTAINED FROM TIME-ACTIVITY CURVES ESTIMATED DIRECTLY FROM NOISELESS CONE BEAM PROJECTIONS USING B-SPLINES OF VARIOUS ORDER AND VARIOUS INITIAL TIME SEGMENT LENGTHS. UNITS FOR UPTAKE k_{21}^m AND WASHOUT k_{12}^m ARE MIN^{-1} . VALUES FOR THE DIMENSIONLESS VASCULAR FRACTION f_v^m AND THE BACKGROUND AMPLITUDE g ARE NOT SHOWN. VALUES THAT DIFFERED FROM THE SIMULATED VALUE BY $\geq 10\%$ ARE SHOWN IN BOLDFACE TYPE

cone beam									
			simulated	noiseless fit					
				initial time segment length (sec)					
				2.5	5	10	20	40	60
cubic B-splines	normal	k_{21}^1	0.700	0.700	0.700	0.701	0.700	0.683	0.709
	myocardium	k_{12}^1	0.150	0.150	0.150	0.150	0.150	0.149	0.155
	septal	k_{21}^2	0.300	0.301	0.301	0.300	0.286	0.181	0.358
	defect	k_{12}^2	0.300	0.301	0.301	0.300	0.288	0.207	0.334
	lateral	k_{21}^3	0.500	0.498	0.496	0.522	0.441	1.17	2.54
	defect	k_{12}^3	0.600	0.599	0.598	0.616	0.565	0.942	1.75
	liver	k_{21}^4	0.900	0.900	0.900	0.900	0.904	0.879	0.873
		k_{12}^4	0.0020	0.0020	0.0020	0.0020	0.0021	0.0016	0.0017
quadratic B-splines	normal	k_{21}^1	0.700	0.701	0.701	0.700	0.700	0.684	0.708
	myocardium	k_{12}^1	0.150	0.150	0.150	0.150	0.150	0.149	0.155
	septal	k_{21}^2	0.300	0.303	0.302	0.300	0.297	0.183	0.350
	defect	k_{12}^2	0.300	0.302	0.301	0.300	0.296	0.211	0.326
	lateral	k_{21}^3	0.500	0.502	0.499	0.502	0.444	1.19	2.89
	defect	k_{12}^3	0.600	0.602	0.598	0.603	0.561	0.957	1.87
	liver	k_{21}^4	0.900	0.900	0.900	0.900	0.901	0.879	0.871
		k_{12}^4	0.0020	0.0020	0.0020	0.0020	0.0020	0.0016	0.0017
linear B-splines	normal	k_{21}^1	0.700	0.703	0.700	0.702	0.698	0.687	0.708
	myocardium	k_{12}^1	0.150	0.150	0.150	0.150	0.150	0.149	0.155
	septal	k_{21}^2	0.300	0.295	0.292	0.308	0.301	0.170	0.335
	defect	k_{12}^2	0.300	0.297	0.296	0.305	0.302	0.204	0.315
	lateral	k_{21}^3	0.500	0.533	0.498	0.491	0.533	1.22	1.90
	defect	k_{12}^3	0.600	0.602	0.578	0.585	0.626	0.990	1.32
	liver	k_{21}^4	0.900	0.903	0.900	0.902	0.895	0.888	0.864
		k_{12}^4	0.0020	0.0020	0.0020	0.0020	0.0020	0.0018	0.0014
constant B-splines	normal	k_{21}^1	0.700	0.688	0.685	0.681	0.682	0.717	0.641
	myocardium	k_{12}^1	0.150	0.146	0.147	0.147	0.148	0.154	0.149
	septal	k_{21}^2	0.300	0.317	0.275	0.265	0.379	0.252	0.082
	defect	k_{12}^2	0.300	0.341	0.299	0.294	0.322	0.254	0.125
	lateral	k_{21}^3	0.500	0.533	0.734	0.665	0.331	1.98	4.23
	defect	k_{12}^3	0.600	0.635	0.833	0.660	0.553	1.36	2.09
	liver	k_{21}^4	0.900	0.911	0.903	0.892	0.885	0.901	0.851
		k_{12}^4	0.0020	0.0027	0.0026	0.0020	0.0021	0.0029	0.0022

where $B(t)$ is the blood input function, k_{21}^m is the uptake parameter, and k_{12}^m is the washout parameter. Total activity in the tissue is given by

$$Q^m(t) + f_v^m B(t) = k_{21}^m V^m(t) + f_v^m B(t) \quad (13)$$

where f_v^m is the fraction of vasculature in the tissue. To fit one-compartment models for the normal myocardium, septal defect,

lateral defect, and liver (denoted by indexes $m = 1, 2, 3$, and 4, respectively), RFIT varies the parameters k_{21}^m , k_{12}^m , and f_v^m to minimize the unweighted sum of squares function

$$\chi_m^2 = \sum_{j=1}^J \sum_{k=1}^K \left\{ \sum_{n=1}^N \hat{a}_{mn} v_{jk}^n - \int_{t_{jk}-\Delta t}^{t_{jk}} [k_{21}^m \hat{V}^m(\tau) + f_v^m \hat{B}(\tau)] d\tau \right\}^2 \quad (14)$$

TABLE IV
SAME QUANTITIES AS IN Table III, FOR PARALLEL BEAM PROJECTIONS. VALUES THAT DIFFERED FROM THE SIMULATED VALUE BY $\geq 10\%$ ARE SHOWN IN BOLDFACE TYPE

parallel beam									
			simulated	noiseless fit					
				initial time segment length (sec)					
				2.5	5	10	20	40	60
cubic B-splines	normal	k_{21}^1	0.700	0.700	0.700	0.701	0.701	0.677	0.718
	myocardium	k_{12}^1	0.150	0.150	0.150	0.150	0.149	0.148	0.158
	septal	k_{21}^2	0.300	0.301	0.301	0.300	0.286	0.162	0.357
	defect	k_{12}^2	0.300	0.301	0.301	0.301	0.287	0.192	0.333
	lateral	k_{21}^3	0.500	0.499	0.494	0.527	0.422	1.48	4.26
	defect	k_{12}^3	0.600	0.599	0.596	0.619	0.551	1.07	2.30
	liver	k_{21}^4	0.900	0.900	0.900	0.900	0.906	0.872	0.867
		k_{12}^4	0.0020	0.0020	0.0020	0.0020	0.0021	0.0015	0.0018
quadratic B-splines	normal	k_{21}^1	0.700	0.701	0.701	0.700	0.700	0.678	0.719
	myocardium	k_{12}^1	0.150	0.150	0.150	0.150	0.150	0.148	0.158
	septal	k_{21}^2	0.300	0.304	0.301	0.301	0.296	0.162	0.347
	defect	k_{12}^2	0.300	0.303	0.301	0.301	0.295	0.194	0.324
	lateral	k_{21}^3	0.500	0.503	0.498	0.507	0.422	1.57	4.64
	defect	k_{12}^3	0.600	0.603	0.597	0.607	0.545	1.12	2.37
	liver	k_{21}^4	0.900	0.900	0.900	0.900	0.903	0.872	0.865
		k_{12}^4	0.0020	0.0020	0.0020	0.0020	0.0020	0.0016	0.0017
linear B-splines	normal	k_{21}^1	0.700	0.704	0.700	0.702	0.697	0.681	0.719
	myocardium	k_{12}^1	0.150	0.150	0.150	0.150	0.150	0.148	0.159
	septal	k_{21}^2	0.300	0.296	0.291	0.309	0.306	0.158	0.327
	defect	k_{12}^2	0.300	0.298	0.296	0.305	0.306	0.194	0.311
	lateral	k_{21}^3	0.500	0.547	0.495	0.474	0.466	1.64	2.71
	defect	k_{12}^3	0.600	0.609	0.574	0.571	0.575	1.18	1.57
	liver	k_{21}^4	0.900	0.904	0.900	0.902	0.895	0.882	0.855
		k_{12}^4	0.0020	0.0020	0.0020	0.0020	0.0020	0.0018	0.0015
constant B-splines	normal	k_{21}^1	0.700	0.679	0.677	0.683	0.682	0.721	0.658
	myocardium	k_{12}^1	0.150	0.144	0.146	0.147	0.148	0.155	0.153
	septal	k_{21}^2	0.300	0.249	0.261	0.259	0.401	0.266	0.071
	defect	k_{12}^2	0.300	0.283	0.289	0.295	0.331	0.251	0.115
	lateral	k_{21}^3	0.500	0.549	0.816	0.682	0.454	3.05	5.74
	defect	k_{12}^3	0.600	0.644	0.892	0.653	0.727	1.70	2.22
	liver	k_{21}^4	0.900	0.912	0.903	0.890	0.879	0.906	0.850
		k_{12}^4	0.0020	0.0028	0.0027	0.0019	0.0020	0.0034	0.0023

where the \hat{a}_{mn} are given by (5), v_{jk}^n is the integral of the n th temporal basis function during the time interval $[t_{jk} - \Delta t, t_{jk}]$ in which projection data are acquired at angle j of rotation k , $\hat{V}^m(\tau)$ is the convolution $\int_0^\tau \hat{B}(\tau') e^{-k_{12}^m(\tau-\tau')} d\tau'$, and $\hat{B}(\tau)$ is derived from the directly estimated blood pool time-activity curve (denoted by index $m = 6$) as follows. Given the set of time integrals, $\{\sum_{n=1}^N \hat{a}_{6n} v_{jk}^n; j = 1, \dots, J; k = 1, \dots, K\}$, of the directly estimated blood pool curve, RFIT models $\hat{B}(\tau)$ as a piecewise linear function that interpolates zero at time $\tau = 0$; the value $\sum_{n=1}^N \hat{a}_{6n} v_{jk}^n / \Delta t$ at time $t_{jk} - (\Delta t/2)$,

for $j = 1, \dots, J$ and $k = 1, \dots, K$; and the value $\sum_{n=1}^N \hat{a}_{6n} v_{jK}^n / \Delta t$ at time t_{jK} .

The amplitude g of the background tissue (denoted by index $m = 5$) is estimated by minimizing the unweighted sum of squares function

$$\chi_5^2 = \sum_{j=1}^J \sum_{k=1}^K \left\{ \sum_{n=1}^N \hat{a}_{5n} v_{jk}^n - \int_{t_{jk}-\Delta t}^{t_{jk}} g \hat{B}(\tau) d\tau \right\}^2. \quad (15)$$

Tables III and IV show the kinetic parameter estimates obtained from the spline models for time-activity curves estimated

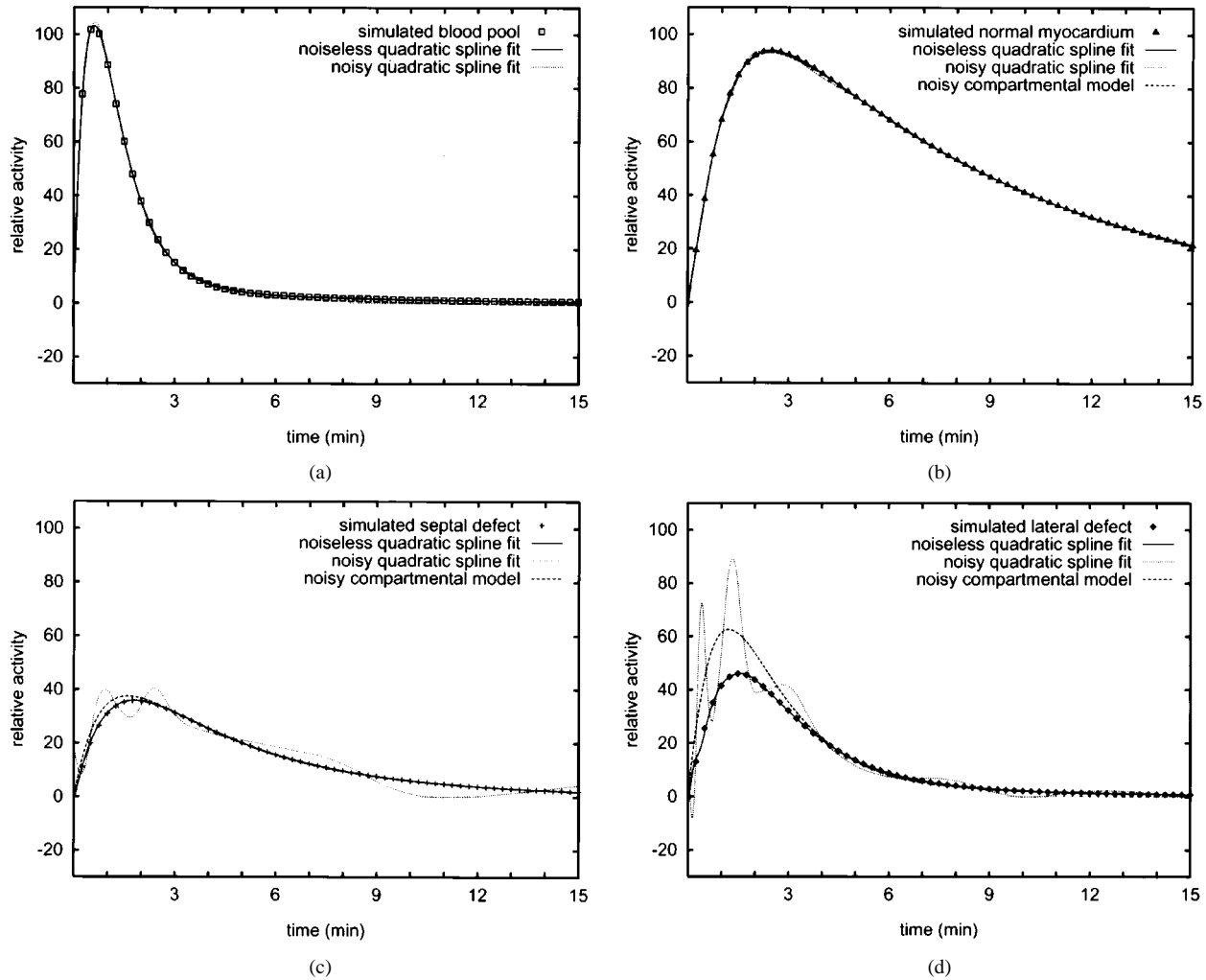


Fig. 7. First of 100 noisy cone beam realizations: time-activity curves for (a) the blood pool, (b) the normal myocardium, (c) the septal defect, and (d) the lateral defect, estimated using quadratic B-splines and an initial time segment length of 10 s [Fig. 4(b)]. Samples of the simulated curves (Fig. 3) are shown as points. The solid and dotted curves were estimated from noiseless and noisy projections, respectively. The dashed curves in (b)–(d) are the kinetic model fits to the noisy curves. The fitted kinetic parameters are listed in column (c) of Table V.

directly from noiseless projections. The biases in the uptake parameters k_{21}^m and the washout parameters k_{12}^m were particularly small when using quadratic B-splines and initial time segment lengths of 2.5, 5, or 10 s. For these three time samplings, the biases (calculated as the absolute value of the difference between the simulated and estimated values, normalized by the simulated value and expressed as a percentage) ranged between 0.0% and 1.0% for the cone beam geometry (Table III) and 0.0% and 1.4% for the parallel beam geometry (Table IV). For cubic B-splines, the biases were comparable, except for the case of the lateral defect and an initial time segment length of 10 s, which had larger bias. For linear B-splines, the biases were comparable for the normal myocardium and the liver, and they were larger for the defects. Overall, the biases for the cubic and linear B-splines ranged between 0.0% and 4.4% and 0.0% and 6.6%, respectively, for the cone beam geometry and initial time segment lengths of 2.5, 5, or 10 s. For the parallel beam geometry, the biases ranged between 0.0% and 5.4% and 0.0% and 9.4%, respectively.

To study the effects of noisy projections on kinetic parameter estimates obtained from spline time-activity curves, 100 real-

izations of projections having Poisson noise were generated for the cone beam and parallel beam geometries. The amplitude of the simulated blood input function was adjusted so that about 10 million events were detected using the cone beam collimators. With this same blood input function, about 6.4 million events were detected using the parallel beam collimators. This number of total detected events was selected to be less, on a slice by slice basis, than the total of 4.8 million events that were detected in the 11 7.12-mm thick slices analyzed in a ^{99m}Tc -teboroxime patient study [8]. Quadratic B-splines and an initial time segment length of 10 s were used to model the time-activity curves. A two-tailed t -test [30] was used to assess the biases in the sample means of the kinetic parameter estimates.

Figs. 7 and 8 show the time-activity curves estimated for the blood pool and the three myocardial volumes of interest, for the first noisy realization of cone beam and parallel beam data, respectively. For both the cone beam and parallel beam geometries, the differences between the spline time-activity curves estimated directly from noiseless and noisy projections were relatively small, for the blood pool and the normal myocardium. For the septal and lateral defects, the differences between the

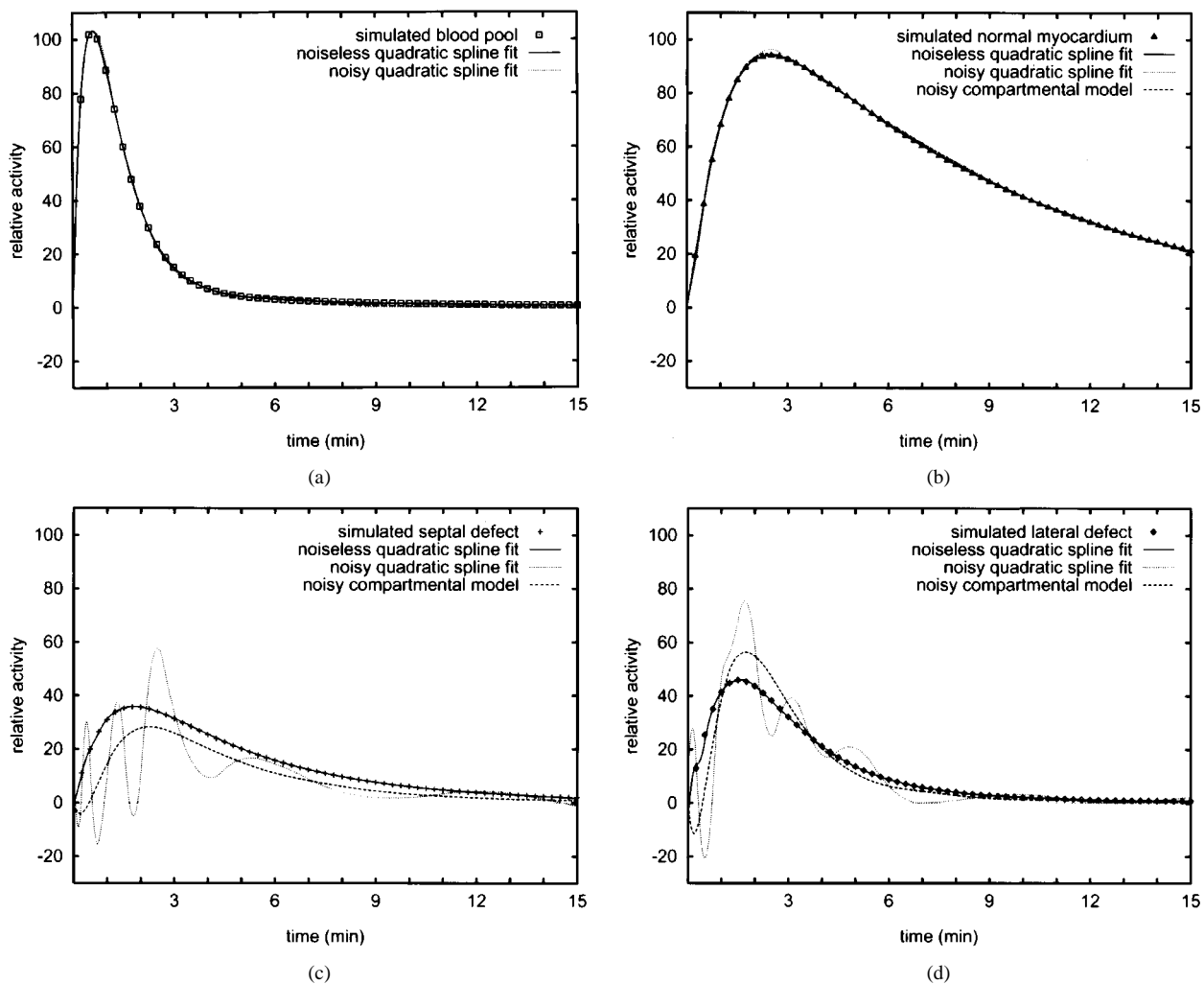


Fig. 8. Same curves as in Fig. 7 for parallel beam projections. The fitted kinetic parameters are listed in column (c) of Table VI.

spline curves estimated directly from noiseless and noisy projections were relatively large. Noise in the spline curve coefficients generated extended excursions (dotted lines) above and below the noiseless spline curves (solid lines). The curves associated with the one-compartment kinetic model fits to the noisy spline curves provided smoother approximations (dashed lines) to the noiseless spline curves. In all cases, the noiseless spline curves provided relatively good fits to the samples of the simulated curves.

Summaries of the results for all 100 noisy realizations are presented in Tables V and VI for the cone beam and parallel beam geometries. For the cone beam geometry (Table V), the sample means [column (d)] of the uptake parameters k_{21}^m and the washout parameters k_{12}^m for the normal myocardium and the liver did not differ significantly from the simulated values ($P > 0.4$). The sample standard deviations [column (e)] ranged between 0.5% and 20%. The sample means of the uptake and washout parameters for the septal and lateral defects were significantly different from the simulated values ($P < 0.05$). The differences between the sample means and the simulated values for the defects ranged between 4.8% and 16%. The sample standard deviations ranged between 22% and 42%.

For the parallel beam geometry (Table VI), the sample means [column (d)] of the uptake parameters k_{21}^m for the

normal myocardium and the liver did not differ significantly from the simulated values ($P > 0.05$). The sample means of the washout parameters k_{12}^m were significantly different from the simulated values ($P < 0.03$), although the difference was only 0.7% for the normal myocardium. The difference for the liver washout was 10%. The sample standard deviations [column (e)] ranged between 0.9% and 40%. The sample means of the uptake and washout parameters for the septal and lateral defects were significantly different from the simulated values ($P < 0.03$). The differences between the sample means and the simulated values for the defects ranged between 11% and 39%. The sample standard deviations ranged between 40% and 140%.

C. Effects of Spatial Segmentation Errors

Having demonstrated that direct time-activity curve estimates and subsequent kinetic parameter estimates are robust with respect to the temporal B-spline basis function order and the initial time sampling, given noiseless data and faithful modeling of the spatial distribution of activity and physical effects, we study now the effects of spatial segmentation errors.

In practice, we expect to base the spatial segmentation on static functional images obtained by summing the late time

TABLE V

KINETIC PARAMETERS OBTAINED FROM TIME-ACTIVITY CURVES ESTIMATED DIRECTLY FROM CONE BEAM PROJECTIONS USING QUADRATIC B-SPLINES AND AN INITIAL TIME SEGMENT LENGTH OF 10 s [Fig. 4(b)]: (a) SIMULATED VALUES; (b) VALUES FROM NOISELESS PROJECTIONS; (c) VALUES FROM THE FIRST OF 100 NOISY REALIZATIONS; (d) SAMPLE MEANS, AND (e) SAMPLE STANDARD DEVIATIONS FOR THE 100 NOISY REALIZATIONS. SAMPLE MEANS THAT WERE SIGNIFICANTLY DIFFERENT FROM THE SIMULATED VALUES (i.e., $P < 0.05$ FOR A TWO-TAILED t -TEST) ARE LABELED WITH ASTERISKS

cone beam						
		simulated	noiseless fit	noisy fits		
				first	sample mean	sample std dev
		(a)	(b)	(c)	(d)	(e)
normal myocardium	k_{21}^1	0.700	0.700	0.697	0.700	0.0064
	k_{12}^1	0.150	0.150	0.151	0.150	0.0016
	f_v^1	0.150	0.150	0.149	0.150	0.011
septal defect	k_{21}^2	0.300	0.300	0.299	0.314*	0.072
	k_{12}^2	0.300	0.300	0.307	0.317*	0.066
	f_v^2	0.100	0.102	0.139	0.095	0.12
lateral defect	k_{21}^3	0.500	0.502	0.628	0.578*	0.21
	k_{12}^3	0.600	0.603	0.727	0.653*	0.16
	f_v^3	0.100	0.096	0.246	0.064*	0.17
liver	k_{21}^4	0.900	0.900	0.901	0.900	0.0046
	k_{12}^4	0.0020	0.0020	0.0029	0.0020	0.0004
	f_v^4	0.200	0.201	0.197	0.201	0.0047
background	g	0.200	0.200	0.199	0.200	0.0010

TABLE VI

SAME QUANTITIES AS IN TABLE V, FOR PARALLEL BEAM PROJECTIONS. SAMPLE MEANS THAT WERE SIGNIFICANTLY DIFFERENT FROM THE SIMULATED VALUES (i.e., $P < 0.05$ FOR A TWO-TAILED t -TEST) ARE LABELED WITH ASTERISKS

parallel beam						
		simulated	noiseless fit	noisy fits		
				first	sample mean	sample std dev
		(a)	(b)	(c)	(d)	(e)
normal myocardium	k_{21}^1	0.700	0.700	0.698	0.702	0.010
	k_{12}^1	0.150	0.150	0.148	0.151*	0.0031
	f_v^1	0.150	0.151	0.148	0.149	0.025
septal defect	k_{21}^2	0.300	0.301	0.322	0.337*	0.16
	k_{12}^2	0.300	0.301	0.397	0.333*	0.12
	f_v^2	0.100	0.100	-0.094	0.086	0.24
lateral defect	k_{21}^3	0.500	0.507	1.102	0.694*	0.68
	k_{12}^3	0.600	0.607	0.954	0.692*	0.40
	f_v^3	0.100	0.092	-0.276	0.059	0.33
liver	k_{21}^4	0.900	0.900	0.894	0.901	0.0082
	k_{12}^4	0.0020	0.0020	0.0014	0.0022*	0.0008
	f_v^4	0.200	0.201	0.198	0.201	0.0081
background	g	0.200	0.200	0.198	0.200	0.0019

frames of the dynamic SPECT study, anatomical images obtained from a transmission scan, and any other images of the patient that may be available (possibly from other modalities, such as X-ray computed tomography). We have developed and applied automated segmentation methods [31], [8], which are being refined and validated as part of our ongoing research.

Even with a perfect segmentation of anatomy, nonuniform activity distributions within individual organs must still be modeled. We consider first the case in which a perfect anatomical segmentation is available, but there is a nonuniform activity distribution in the myocardium caused by defects. We then perform a preliminary investigation into the errors resulting

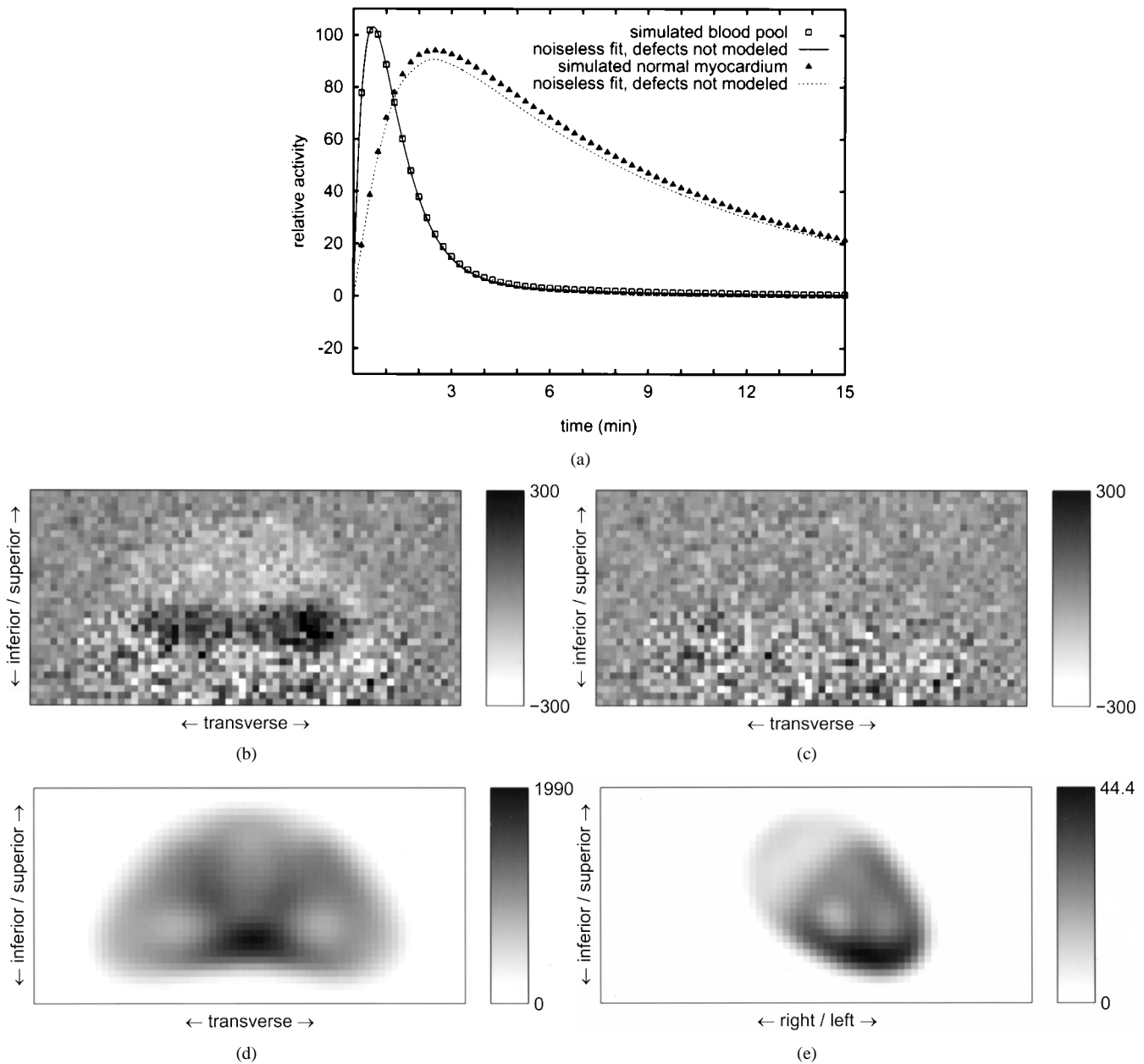


Fig. 9. Effects of failure to segment myocardial defects. The underestimation of (a) time-activity curves estimated from noiseless data with no modeling of defects; summed residuals for noisy data and (b) no modeling and (c) faithful modeling of defects; (d) summed noiseless projections and, (e) summed noiseless anterior projections for myocardium with defects. The underestimation of myocardial activity seen in (a) results in spatial structure in the summed residuals corresponds to the myocardium in (d), (e). In (b)–(d), the summation is over all 120 angles for each of the 15 rotations, whereas in (e), the summation is over one angle per rotation. The increased noise levels in the lower portions of (b), (c) are because of the relatively high-activity concentration in the liver.

from inaccurate localization of the myocardial walls for a defect-free heart.

1) Failure to Segment Myocardial Defects: Using quadratic B-splines and an initial time segment length of 10 s, time-activity curves were estimated from noiseless simulated cone beam data generated using the MCAT phantom having defects in the septal and lateral walls of the left ventricular myocardium [Fig. 2(a)]. However, the myocardial defects were not included in the spatial segmentation used for estimating the time-activity curves, and the activity distribution was assumed instead to be uniform throughout the entire myocardium.

Because of this failure to segment the myocardial defects, the time-activity curve estimated for the myocardium was system-

atically low [Fig. 9(a)] and had an rms error of 4.9%, compared with the error of 0.091% achieved using the faithful spatial segmentation [Fig. 5(b)]. The rms error for the blood pool curve increased from 0.48% to 1.8%.

Using these time-activity curves, the estimates of the myocardial uptake and washout parameters were $k_{21} = 0.670 \text{ min}^{-1}$ and $k_{12} = 0.146 \text{ min}^{-1}$, respectively, compared with the unbiased estimates $k_{21} = 0.700 \text{ min}^{-1}$ and $k_{12} = 0.150 \text{ min}^{-1}$ obtained from the curves estimated using the faithful spatial segmentation (Table III).

Despite these relatively small errors in quantitation, spatial structure was evident in the residuals for the modeled projections, even for simulated noisy projection data containing 10

million detected events [Fig. 9(b)]. Thus, it may be possible in practice to detect spatial model mismatch resulting from the failure to segment small myocardial defects, as well as to refine the segmentation iteratively in an effort to reduce the spatial structure in the residuals for the modeled projections.

2) *Inaccurate Localization of the Myocardial Walls:* Using quadratic B-splines and an initial time segment length of 10 s, time-activity curves were estimated from noiseless simulated cone beam data generated using the MCAT phantom with a defect-free myocardium. Spatial model mismatches were induced by either dilating or eroding the endocardial wall, or dilating or eroding the epicardial wall. The wall location was displaced by about 2.5 mm in each case by applying three-dimensional (3-D) gray-scale dilation or erosion operators [32] as appropriate to voxel maps of the indicator functions for the blood pool, myocardium, and background tissue, before forward projecting the volumes to calculate the spatial basis projection factors u_{ij}^m .

The rms errors for the time-activity curves estimated using these incorrect spatial segmentations ranged between 15% and 23% for the myocardium and 2.8% and 30% for the blood pool. The kinetic model parameters obtained from these curves ranged between 0.537 and 0.961 min^{-1} for the uptake k_{21} and 0.051 and 0.288 min^{-1} for the washout k_{12} , compared with the unbiased estimates $k_{21} = 0.700 \text{ min}^{-1}$ and $k_{12} = 0.150 \text{ min}^{-1}$ obtained from curves estimated using the faithful spatial segmentation. In each case, spatial structure was evident in the residuals for the modeled projections for simulated noisy projection data containing 10 million detected events (Fig. 10).

Thus, it appears that systematic errors in the gross segmentation of anatomy may have a larger effect on quantitation than does the failure to account for small nonuniformities in the activity distributions within the individual organs. Further study is needed to assess the accuracy with which the spatial segmentation can be performed in practice. As was the case with the failure to segment small myocardial defects, it may be possible in practice to detect spatial model mismatch resulting from gross myocardial segmentation errors, as well as to refine the segmentation iteratively in an effort to reduce the spatial structure in the residuals for the modeled projections.

IV. DISCUSSION

The combination of gantry motion and the time-variation of the radiopharmaceutical distribution being imaged results in inconsistent dynamic SPECT projection data sets. In addition, the use of cone beam collimators can result in insufficient, as well as truncated, projection samples. Conventional kinetic model parameter estimation from time-activity curves generated by overlaying volumes of interest on images reconstructed from these projection data results in biases. The biases in the time-activity curve estimates and the subsequent kinetic model parameter estimates can be reduced significantly by estimating the time-activity curves directly from the projections. Implementation of this strategy requires a spatial and temporal model of the radiopharmaceutical distribution throughout the projected field of view.

Computational issues associated with fully 4-D direct estimation of spatiotemporal distributions from dynamic SPECT

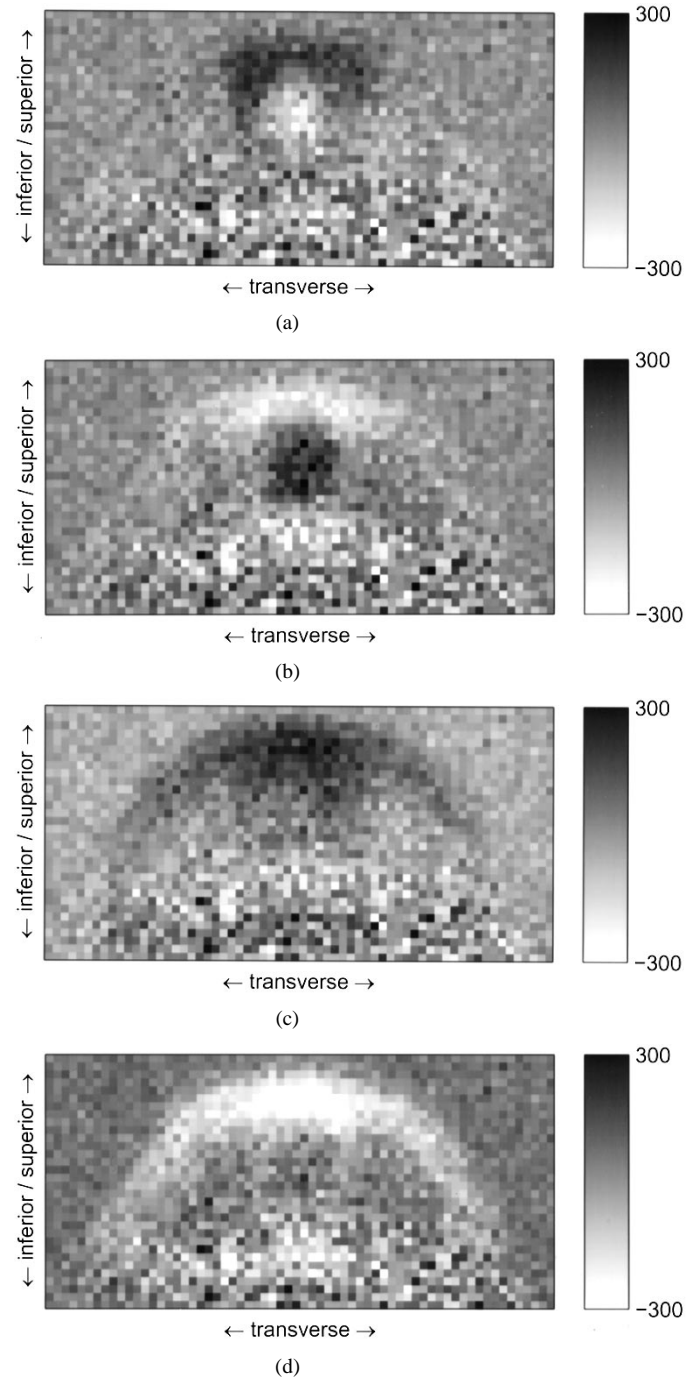


Fig. 10. Effects of inaccurate localization of the myocardial walls: summed residuals for noisy data and (a) dilated endocardium, (b) eroded endocardium, (c) dilated epicardium, and (d) eroded epicardium. In (a)–(d), the summation is over all 120 angles for each of the 15 rotations. The increased noise levels in the lower portions of (a)–(d) are because of the relatively high-activity concentration in the liver.

projection data have been addressed, so that least-squares estimates of time-activity curves can be obtained quickly and accurately using a workstation with a modest amount of memory. Temporal B-splines were used to model the time-activity curves for the blood pool and tissue volumes in simulated cone beam and parallel beam cardiac data acquisitions. For noiseless data, there were only minor differences between the curve models estimated from the cone beam and the parallel beam data, as well as minor differences between subsequent kinetic model

parameter estimates. The direct time-activity curve estimates and subsequent kinetic parameter estimates were robust with respect to the temporal B-spline basis function order and the initial time sampling, given noiseless data and faithful modeling of the spatial distribution of activity and physical effects. For both the cone beam and parallel beam geometries, rms modeling errors for the time-activity curves were less than 7% when using cubic, quadratic, or linear splines with initial time segment lengths of 2.5, 5, or 10 s. Errors in uptake and washout parameters for one-compartment kinetic models obtained from these spline curves were less than 10%.

For small (3-cm diameter) myocardial defect regions exhibiting reduced uptake and accelerated washout, biased estimates of kinetic parameters for one-compartment models were obtained for noisy data using quadratic B-splines and an initial time sampling of 10 s. The uptake and washout parameter estimates obtained from noisy cone beam data had less bias (4.8%–16%) and variance (22%–42%) than did those obtained from noisy parallel beam data (bias of 11%–39%; variance of 40%–140%). This was presumably because of the increased sensitivity of the cone beam collimators and their increased resolution at the center of tomograph, near which the defects were imaged.

What remains to be investigated in more detail are the effects of the B-spline order and the initial time sampling on kinetic parameters obtained from time-activity curves estimated directly from noisy projection data, as well as the impact of errors in modeling the spatial distribution of activity and physical effects. For most of our simulations, we have assumed that we have a perfect segmentation of a piecewise uniform activity distribution, faithful models for attenuation and geometric point response, and that there is no scatter. Clearly, quantitative accuracy will suffer in practice, when we have only approximate models for the spatial distribution of activity (as in Section III-C) and physical effects.

Further study is needed to assess the accuracy with which the spatial segmentation can be performed in practice. Even with a perfect segmentation of anatomy, nonuniform activity distributions within individual organs must still be modeled. For the case in which the activities are modeled to be uniform within the individual volumes of the segmentation, this requires subdividing the segmentation into smaller volumes. A second approach is to model nonuniform activities within the larger volumes by selecting sets of spatial basis functions defined within the larger volumes (e.g., spherical harmonics defined within the left ventricular myocardium). Our future research in this area will focus on the second approach, used in conjunction with adaptive refinement of the volume boundaries. Our future research will also focus on improved modeling of physical effects, particularly attenuation and scatter.

Although accurate, precise quantitation is the ultimate goal, inaccuracy and imprecision can be tolerated so long as we can discriminate between healthy and diseased tissue. For example, although our noisy data simulations yielded biased estimates of uptake and washout parameters for the small myocardial defect regions, the resulting kinetics were significantly different from the kinetics obtained for the normal myocardium. Given estimates of time-activity curves or kinetic parameters for two vol-

umes of interest, as well as estimates of the uncertainties and correlations of the quantities and a measure of the goodness of fit of the overall spatiotemporal model, we are at least in a position to make an objective comparison that can supplement a subjective evaluation of the data.

The estimation of time-activity curves directly from projection data appears to be potentially useful for clinical SPECT studies involving slowly rotating gantries, particularly those that use a single-detector system or body contouring orbits with a multidetector system. The computationally efficient methodology presented in Section II facilitates continued research in this area. The algorithm developed in Section II can also be used to solve quickly the linear least-squares subproblem embedded in the nonlinear estimation problem that we formulated in [5]–[7], thereby facilitating future research into estimating kinetic parameters directly from projection data. This includes the joint estimation of a temporal model for the blood input function and kinetic parameters for compartmental models directly from projection data, as well as the parameterization of spatially nonuniform activity concentrations within segmented volumes encompassing the projected field of view.

ACKNOWLEDGMENT

The authors thank Dr. G. Zeng for his helpful advice, and the University of North Carolina Medical Imaging Research Laboratory for making the MCAT phantom available. They also thank the reviewers for their comments and suggestions, which helped to improve the exposition. Some preliminary results of this work were presented in the conference report [33].

REFERENCES

- [1] H. K. Tuy, "An inversion formula for cone-beam reconstruction," *SIAM J. Appl. Math.*, vol. 43, no. 3, pp. 546–552, 1983.
- [2] G. T. Gullberg, R. H. Huesman, S. G. Ross, E. V. R. Di Bella, G. L. Zeng, B. W. Reutter, P. E. Christian, and S. A. Foresti, "Dynamic cardiac single-photon emission computed tomography," in *Nuclear Cardiology: State of the Art and Future Directions*, B. L. Zaret and G. A. Beller, Eds. St. Louis, MO: Mosby, 1999, ch. 11, pp. 137–187.
- [3] R. E. Carson, "A maximum likelihood method for region-of-interest evaluation in emission tomography," *J. Comput. Assist. Tomogr.*, vol. 10, no. 4, pp. 654–663, 1986.
- [4] A. R. Formiconi, "Least squares algorithm for region-of-interest evaluation in emission tomography," *IEEE Trans. Med. Imag.*, vol. 12, no. 1, pp. 90–100, 1993.
- [5] R. H. Huesman, B. W. Reutter, G. L. Zeng, and G. T. Gullberg, "Kinetic parameter estimation from SPECT projection measurements," *J. Nucl. Med.*, vol. 38, no. 5, pp. 222P–223P, 1997.
- [6] —, "Kinetic parameter estimation from SPECT cone-beam projection measurements," *Phys. Med. Biol.*, vol. 43, no. 4, pp. 973–982, 1998.
- [7] B. W. Reutter, G. T. Gullberg, and R. H. Huesman, "Kinetic parameter estimation from attenuated SPECT projection measurements," *IEEE Trans. Nucl. Sci.*, vol. 45, no. 6, pp. 3007–3013, 1998.
- [8] —, "Kinetic parameter estimation from dynamic cardiac patient SPECT projection measurements," in *1998 IEEE Nucl. Sci. Symp. Med. Imag. Conf. Rec.*, R. Sudharsanan, Ed., 1999, pp. 1953–1958.
- [9] P. C. Chiao, W. L. Rogers, N. H. Clinthorne, J. A. Fessler, and A. O. Hero, "Model-based estimation for dynamic cardiac studies using ECT," *IEEE Trans. Med. Imag.*, vol. 13, pp. 217–226, Feb. 1994.
- [10] P. C. Chiao, W. L. Rogers, J. A. Fessler, N. H. Clinthorne, and A. O. Hero, "Model-based estimation with boundary side information or boundary regularization," *IEEE Trans. Med. Imag.*, vol. 13, pp. 227–234, Feb. 1994.
- [11] R. E. Carson, "Two image-wide parameter estimation methods for positron emission tomography: Theory and application to the measurement of local cerebral blood flow in humans," Ph.D. dissertation, University of California, Los Angeles, 1983.

- [12] D. L. Snyder, "Parameter estimation for dynamic studies in emission-tomography systems having list-mode data," *IEEE Trans. Nucl. Sci.*, vol. 31, no. 2, pp. 925–931, 1984.
- [13] F. O'Sullivan, "Imaging radiotracer model parameters in PET: A mixture analysis approach," *IEEE Trans. Med. Imag.*, vol. 12, pp. 399–412, Mar. 1993.
- [14] S. R. Meikle, J. C. Matthews, V. J. Cunningham, D. L. Bailey, L. Livieratos, T. Jones, and P. Price, "Parametric image reconstruction using spectral analysis of PET projection data," *Phys. Med. Biol.*, vol. 43, no. 3, pp. 651–666, 1998.
- [15] H. H. Bauschke, D. Noll, A. Celler, and J. M. Borwein, "An EM algorithm for dynamic SPECT," *IEEE Trans. Med. Imag.*, vol. 18, no. 3, pp. 252–261, 1999.
- [16] T. Farncombe, A. Celler, D. Noll, J. Maeght, and R. Harrop, "Dynamic SPECT imaging using a single camera rotation (dSPECT)," *IEEE Trans. Nucl. Sci.*, vol. 46, no. 4, pp. 1055–1061, 1999.
- [17] R. H. Bartels, J. C. Beatty, and B. A. Barsky, *An Introduction to Splines for use in Computer Graphics and Geometric Modeling*. Los Altos, CA: Kaufman, 1987.
- [18] K. Chen, S. C. Huang, and D. C. Yu, "The effects of measurement errors in the plasma radioactivity curve on parameter estimation in positron emission tomography," *Phys. Med. Biol.*, vol. 36, no. 9, pp. 1183–1200, 1991.
- [19] T. E. Nichols, J. Qi, and R. M. Leahy, "Continuous time dynamic PET imaging using list mode data," in *Inform. Proc. Med. Imag.: Proc. 16th Int. Conf.*, A. Kuba, M. Šámal, and A. Todd-Pokropek, Eds., 1999, pp. 98–111.
- [20] W. H. Press, S. A. Teukolsky, W. T. Vetterling, and B. P. Flannery, *Numerical Recipes in Fortran 90: The Art of Parallel Scientific Computing*. Cambridge, U.K.: Cambridge Univ. Press, 1996.
- [21] R. H. Huesman and B. M. Mazoyer, "Kinetic data analysis with a noisy input function," *Phys. Med. Biol.*, vol. 32, no. 12, pp. 1569–1579, 1987.
- [22] B. M. W. Tsui, J. A. Terry, and G. T. Gullberg, "Evaluation of cardiac cone-beam single photon emission computed tomography using observer performance experiments and receiver operating characteristic analysis," *Invest. Radiol.*, vol. 28, no. 12, pp. 1101–1112, 1993.
- [23] R. K. Narra, T. Feld, and A. D. Nunn, "Absorbed radiation dose to humans from technetium-99m-teboroxine," *J. Nucl. Med.*, vol. 33, no. 1, pp. 88–93, 1992.
- [24] A. M. Smith, G. T. Gullberg, P. E. Christian, and F. L. Diaz, "Kinetic modeling of teboroxine using dynamic SPECT imaging of a canine model," *J. Nucl. Med.*, vol. 35, no. 3, pp. 484–495, 1994.
- [25] A. M. Smith, G. T. Gullberg, and P. E. Christian, "Experimental verification of technetium 99m-labeled teboroxine kinetic parameters in the myocardium with dynamic single-photon emission computed tomography: Reproducibility, correlation to flow, and susceptibility to extravascular contamination," *J. Nucl. Cardiol.*, vol. 3, no. 2, pp. 130–142, 1996.
- [26] G. L. Zeng, G. T. Gullberg, B. M. W. Tsui, and J. A. Terry, "Three-dimensional iterative reconstruction algorithms with attenuation and geometric point response correction," *IEEE Trans. Nucl. Sci.*, vol. 38, no. 2, pp. 693–702, 1991.
- [27] B. M. Mazoyer, R. H. Huesman, T. F. Budinger, and B. L. Knittel, "Dynamic PET data analysis," *J. Comput. Assist. Tomogr.*, vol. 10, no. 4, pp. 645–653, 1986.
- [28] P. G. Coxson, E. M. Salmeron, R. H. Huesman, and B. M. Mazoyer, "Simulation of compartmental models for kinetic data from a position emission tomograph," *Comput. Methods Programs Biomed.*, vol. 37, no. 3, pp. 205–214, 1992.
- [29] R. H. Huesman, B. L. Knittel, B. M. Mazoyer, P. G. Coxson, E. M. Salmeron, G. J. Klein, B. W. Reutter, and T. F. Budinger, "Notes on RFIT: A program for fitting compartmental models to region-of-interest dynamic emission tomographic data," Lawrence Berkeley National Laboratory, Berkeley, CA, LBL-37 621, 1995.
- [30] M. H. DeGroot, *Probability and Statistics*. Reading, MA: Addison Wesley, 1986.
- [31] B. W. Reutter, G. J. Klein, and R. H. Huesman, "Automated 3-D segmentation of respiratory-gated PET transmission images," *IEEE Trans. Nucl. Sci.*, vol. 44, no. 6, pp. 2473–2476, 1997.
- [32] S. R. Sternberg, "Grayscale morphology," *Comput. Vision Graphics Imag. Process.*, vol. 35, no. 3, pp. 333–335, 1986.
- [33] B. W. Reutter, G. T. Gullberg, and R. H. Huesman, "Direct least squares estimation of spatiotemporal distribution from dynamic cardiac SPECT projections," in *1999 IEEE Nucl. Sci. Symp. Med. Imag. Conf. Rec.*, J. A. Seibert, Ed., 2000, pp. 1114–1118.